

Finite-size effects in cylindrical topological insulators

Michele Governale¹, Bibek Bhandari², Fabio Taddei³,
Ken-Ichiro Imura⁴ and Ulrich Zülicke¹

¹School of Chemical and Physical Sciences and MacDiarmid Institute for Advanced Materials and Nanotechnology, Victoria University of Wellington, PO Box 600, Wellington 6140, New Zealand

²Scuola Normale Superiore & NEST, NANO-CNR, Pisa, Italy

³NEST, NANO-CNR & Scuola Normale Superiore, Pisa, Italy

⁴Department of Quantum Matter, AdSM, Hiroshima University, Higashi-Hiroshima 739-8530, Japan

E-mail: michele.governale@vuw.ac.nz

Abstract. We present a theoretical study of a nanowire made of a three-dimensional topological insulator. The bulk topological insulator is described by a continuum-model Hamiltonian, and the cylindrical-nanowire geometry is modelled by a hard-wall boundary condition. We provide the secular equation for the eigenenergies of the systems (both for bulk and surface states) and the analytical form of the energy eigenfunctions. We describe how the surface states of the cylinder are modified by finite-size effects. In particular, we provide a $1/R$ expansion for the energy of the surface states up to second order. The knowledge of the analytical form for the wavefunctions enables the computation of matrix elements of any single-particle operators. In particular, we compute the matrix elements of the optical dipole operator, which describe optical absorption and emission, treating intra- and inter-band transition on the same footing. Selection rules for optical transitions require conservation of linear momentum parallel to the nanowire axis, and a change of 0 or ± 1 in the total-angular-momentum projection parallel to the nanowire axis. The magnitude of the optical-transition matrix elements is strongly affected by the finite radius of the nanowire.

1. Introduction

Three-dimensional (3D) topological insulators (TI)s were predicted in 2007 [1] as electronic systems characterized by an insulating bulk and gapless conducting surface states (for a review, see Refs. [2–5]). The states at the interface between the system and the vacuum are topologically protected against time-reversal invariant perturbations and consist, at low energy, of single Dirac fermions [6–8]. Recent advances in nanofabrication techniques have enabled the realization of 3D-TI samples of reduced dimensionality, for example in the form of nanowires [9–26]. 3D-TI nanowires proximised with an s-wave superconductor have been proposed as a possible platform for the realization of Majorana bound states [27, 28]. The availability of nanometer-scale samples is interesting also because it offers the opportunity to investigate the competition between the inverted bulk gap and the size-quantisation energy as well as the extent of the localization of surface states [29–38]. In Ref. [29], an approximate analytic model supplemented by a numerical scheme based on exact diagonalisation was introduced to study the quantum interference effects on the low-energy spectrum of Bi_2Se_3 nanowires.

In this paper we explore the properties of a finite-radius 3D-TI cylinder, using the envelope-function description of the TI bulk band structure developed in Refs. [39, 40]. Our goal is to determine the dependence of its energy spectrum and eigenfunctions on the radius R . The central point of our analysis is the analytical expression of the eigenfunctions, which allow us to express cylindrical hard-wall boundary conditions in terms of secular equations that can be approximated in the limit of large radii: we obtain approximate expressions for the eigenenergies up to second order in $1/R$. The analytical functional form of the eigenfunctions, which is valid irrespective of the radius of the wire, enables the calculation of the matrix elements of any observable. As an example, we consider the dipole matrix elements for optical transitions. In particular, we find that the selection rules for absorption and emission are not modified by a finite radius, in contrast to the case of a spherical nanoparticle [36]. Numerical results are presented for two different materials, namely Bi_2Se_3 and Bi_2Te_3 , which show qualitatively different behaviours. We compute eigenenergies as functions of the radius R and longitudinal momentum and compare them with approximate large-radius expressions. The eigenenergies are found to be oscillating for small values of R , especially in the case of Bi_2Te_3 . Moreover, we characterize the behaviour of eigenfunctions by plotting the average radial coordinate and the corresponding variance as a function of the radius R . As expected, the average coordinate moves towards the centre of the nanowire for small values of R , more rapidly for Bi_2Te_3 than for Bi_2Se_3 , while the variance increases in an oscillating fashion for increasing radii, reaching the asymptotic value more rapidly in the case of Bi_2Se_3 with respect to Bi_2Te_3 . Finally, we calculate numerically the dependence of the optical dipole matrix elements on the radius finding quantitative important changes with respect to the bulk situation.

The paper is organized as follows. In section 2, we present an analytic treatment for a cylindrical 3D-TI nanowire with hard-wall confinement. We conclude section 2

with a complete analytic expression for the eigenfunction of the finite-radius 3D-TI. In section 3, we study the finite size effects on the topological properties of a cylindrical 3D-TI for two different materials. Specifically, we study the eigenenergies and characterise the eigenfunctions of the system as a function of the radius of the cylinder. Finally, in section 3.3, we calculate the optical dipole matrix elements of a cylindrical TI and study their dependence on the the radius of the cylinder.

2. Model

We consider an infinitely long cylinder of TI of radius R , whose axis is in the z -direction. The bulk TI is described by the Hamiltonian [39, 40]

$$H_0 = \begin{pmatrix} m(\mathbf{p}) & Bp_z & 0 & Ap_- \\ Bp_z & -m(\mathbf{p}) & Ap_- & 0 \\ 0 & Ap_+ & m(\mathbf{p}) & -Bp_z \\ Ap_+ & 0 & -Bp_z & -m(\mathbf{p}) \end{pmatrix}, \quad (1)$$

where $\mathbf{p} = (p_x, p_y, p_z)$ is the momentum operator, $m(\mathbf{p}) = m_0 + m_1 p_z^2 + m_2 (p_x^2 + p_y^2)$ is the mass term and $p_{\pm} = p_x \pm ip_y$. The Hamiltonian (1) is written in the basis $\{|P1_z^+ \uparrow\rangle, |P2_z^- \uparrow\rangle, |P1_z^+ \downarrow\rangle, |P2_z^- \downarrow\rangle\}$. When the sign of m_0/m_2 is negative, the material is in the topological insulating phase, causing isolated boundaries to host surface states represented by gapless Dirac cones. The coefficients m_0 , m_1 and m_2 , as well as the coefficients A and B of the linear-momentum terms depend on the material [41]. The values of the parameters for the most common TIs are reported in Table 1. As the system

Table 1. Values for parameters in the effective continuum-model Hamiltonian describing bulk-electronic states of currently available topological-insulator materials, from Ref [41].

	Bi ₂ Se ₃	Bi ₂ Te ₃	Sb ₂ Te ₃
m_0 (eV)	-0.169	-0.296	-0.182
m_1 (eVÅ ²)	3.353	9.258	22.136
m_2 (eVÅ ²)	29.375	177.355	51.320
B (eVÅ)	1.836	0.900	1.174
A (eVÅ)	2.513	4.003	3.694

has cylindrical symmetry, it is convenient to express H_0 in cylindrical coordinates. Following Imura *et al.* [42], we write the Hamiltonian as a sum of two terms

$$H_0 = H_{\perp} + H_{\parallel} \quad , \quad (2)$$

where

$$H_{\perp} = \begin{pmatrix} m_{\perp} & 0 & 0 & -iAe^{-i\varphi}\partial_{\rho} \\ 0 & -m_{\perp} & -iAe^{-i\varphi}\partial_{\rho} & 0 \\ 0 & -iAe^{i\varphi}\partial_{\rho} & m_{\perp} & 0 \\ -iAe^{i\varphi}\partial_{\rho} & 0 & 0 & -m_{\perp} \end{pmatrix} \quad (3a)$$

$$H_{\parallel} = \begin{pmatrix} m_{\parallel} & Bp_z & 0 & -\frac{A}{\rho}e^{-i\varphi}\partial_{\varphi} \\ Bp_z & -m_{\parallel} & -\frac{A}{\rho}e^{-i\varphi}\partial_{\varphi} & 0 \\ 0 & \frac{A}{\rho}e^{i\varphi}\partial_{\varphi} & m_{\parallel} & -Bp_z \\ \frac{A}{\rho}e^{i\varphi}\partial_{\varphi} & 0 & -Bp_z & -m_{\parallel} \end{pmatrix} \quad (3b)$$

and with the mass terms given by the expressions

$$m_{\perp} = m_0 + m_2 \left(-\partial_{\rho}^2 - \frac{1}{\rho}\partial_{\rho} \right) \quad (4)$$

$$m_{\parallel} = -m_2 \frac{1}{\rho^2} \partial_{\varphi}^2 + m_1 p_z^2. \quad (5)$$

The Hamiltonian H_0 commutes both with p_z and with the z -component of the total angular momentum $(L_z + \frac{\hbar}{2}\sigma_z) \otimes \tau_0$, where τ_0 is the identity matrix in the orbital pseudo-spin subspace. In the following, to avoid cluttering the notation, we set $\hbar = 1$. The commutation relations of H_0 discussed above suggest the following *Ansatz* for the wave function:

$$\Psi(\rho, \varphi, z) = \frac{e^{ik_z z}}{\sqrt{2\pi}} \begin{pmatrix} \Phi_1(\rho)e^{i(j-\frac{1}{2})\varphi} \\ \Phi_2(\rho)e^{i(j-\frac{1}{2})\varphi} \\ \Phi_3(\rho)e^{i(j+\frac{1}{2})\varphi} \\ \Phi_4(\rho)e^{i(j+\frac{1}{2})\varphi} \end{pmatrix}, \quad (6)$$

where k_z is the eigenvalue of p_z and j (half integer) the eigenvalue of the z component of the total angular momentum. Solving the eigensystem requires applying the Hamiltonian Eq. (1) to the wavefunction in Eq. (6). The calculation is detailed in [Appendix A](#). In order to solve the radial part of the eigensystem, we make further *Ansätze* for the $\Phi_i(\rho)$ and rewrite Eq. (6) as

$$\Psi(\rho, \varphi, z) = \frac{e^{ik_z z}}{\sqrt{2\pi}} \begin{pmatrix} c_1 J_{j-\frac{1}{2}}(\kappa\rho)e^{i(j-\frac{1}{2})\varphi} \\ c_2 J_{j-\frac{1}{2}}(\kappa\rho)e^{i(j-\frac{1}{2})\varphi} \\ c_3 J_{j+\frac{1}{2}}(\kappa\rho)e^{i(j+\frac{1}{2})\varphi} \\ c_4 J_{j+\frac{1}{2}}(\kappa\rho)e^{i(j+\frac{1}{2})\varphi} \end{pmatrix}, \quad (7)$$

where $J_n(z)$ is a Bessel function of the first kind and κ and the coefficients c_1, \dots, c_4 need to be determined. In order for the *Ansatz* of Eq. (7) to be an eigenfunction of H_0 with energy E , the parameter κ needs to take one of the following two values

$$\kappa_{\pm} = \left[- \left(\frac{m_0}{m_2} + \frac{A^2}{2m_2^2} + \frac{m_1 k_z^2}{m_2} \right) \pm \sqrt{\frac{A^4}{4m_2^4} + \frac{E^2}{m_2^2} + \frac{A^2 m_0}{m_2^3} + \left(\frac{A^2}{m_2^2} \frac{m_1}{m_2} - \frac{B^2}{m_2^2} \right) k_z^2} \right]^{1/2}. \quad (8)$$

For the coefficients $(c_1, c_2, c_3, c_4)^T$ there are four independent solutions (two for κ_+ and two for κ_-) given by

$$\left(\frac{iA\kappa_{\pm}}{\Delta_{\pm}}, 0, \frac{Bk_z}{\Delta_{\pm}}, 1 \right)^T, \left(-\frac{Bk_z}{\Delta_{\pm}}, 1, -\frac{iA\kappa_{\pm}}{\Delta_{\pm}}, 0 \right)^T, \quad (9)$$

where $\Delta_{\pm} = m_2\kappa_{\pm}^2 + m_1k_z^2 + m_0 - E$. The general solution for the wavefunction with quantum numbers k_z, j and E is a linear combination of the four independent solutions obtained above:

$$\Psi(\rho, \varphi, z) = \frac{e^{ik_z z}}{\sqrt{2\pi}} \sum_{s=\pm} \left\{ \alpha_s \begin{pmatrix} \frac{iA\kappa_s}{\Delta_s} J_{j-\frac{1}{2}}(\kappa_s\rho) e^{i(j-\frac{1}{2})\varphi} \\ 0 \\ \frac{Bk_z}{\Delta_s} J_{j+\frac{1}{2}}(\kappa_s\rho) e^{i(j+\frac{1}{2})\varphi} \\ J_{j+\frac{1}{2}}(\kappa_s\rho) e^{i(j+\frac{1}{2})\varphi} \end{pmatrix} + \beta_s \begin{pmatrix} -\frac{Bk_z}{\Delta_s} J_{j-\frac{1}{2}}(\kappa_s\rho) e^{i(j-\frac{1}{2})\varphi} \\ J_{j-\frac{1}{2}}(\kappa_s\rho) e^{i(j-\frac{1}{2})\varphi} \\ -\frac{iA\kappa_s}{\Delta_s} J_{j+\frac{1}{2}}(\kappa_s\rho) e^{i(j+\frac{1}{2})\varphi} \\ 0 \end{pmatrix} \right\}. \quad (10)$$

We can now solve the confinement problem by assuming a hard-wall cylindrical confinement potential of radius R . We need to impose the boundary condition $\Psi(R, \varphi, z) = 0$. This leads to a system of equations for the coefficients α_s and β_s which has non-trivial solutions for energies obeying the secular equation

$$\frac{T_j(\kappa_+R)}{T_j(\kappa_-R)} + \frac{T_j(\kappa_-R)}{T_j(\kappa_+R)} = \frac{\kappa_+ \Delta_-}{\kappa_- \Delta_+} + \frac{\kappa_- \Delta_+}{\kappa_+ \Delta_-} + \frac{B^2}{A^2} k_z^2 \frac{(\Delta_+ - \Delta_-)^2}{\kappa_+ \kappa_- \Delta_+ \Delta_-}, \quad (11)$$

where we have defined the function $T_j(z) = \frac{J_{j+1/2}(z)}{J_{j-1/2}(z)}$. A detailed derivation of the secular equation is provided in [Appendix A](#). In the case $k_z = 0$, the problem decouples in two 2×2 problems and we have two independent secular equations

$$\frac{\kappa_+ \Delta_-}{\kappa_- \Delta_+} = \frac{T_j(\kappa_+R)}{T_j(\kappa_-R)}, \quad (12a)$$

$$\frac{\kappa_+ \Delta_-}{\kappa_- \Delta_+} = \frac{T_j(\kappa_-R)}{T_j(\kappa_+R)}, \quad (12b)$$

which are analogous to Eq. (28) of Ref. [36]. The $k_z = 0$ energy eigenstates associated with solutions of Eq. (12a) have $\beta_s = 0$ and therefore their only nonvanishing spinor components are the first and the fourth. Conversely, the eigenstates corresponding to solutions of Eq. (12b) have $\alpha_s = 0$ and therefore their only nonvanishing spinor components are the second and the third. Taking into account the transformation properties of the basis states under spatial inversion, it is straightforward to show that eigenstates associated with energy eigenvalues arising from the secular equation (12a) [(12b)] are also parity eigenstates with eigenvalue $(-1)^{j-\frac{1}{2}}$ [$(-1)^{j+\frac{1}{2}}$].

Even for finite k_z , the spinors multiplied by α_s [β_s] in the *Ansatz* (10) remain parity eigenstates with eigenvalue $(-1)^{j-\frac{1}{2}}$ [$(-1)^{j+\frac{1}{2}}$]. However, as the energy eigenstates for nonzero k_z are superpositions of these opposite-parity spinors, they are not eigenstates of parity.

Once we fix the quantum number j and k_z and solve the secular equation (11) we obtain a series of solutions both with positive and negative energies. Of these, we will only consider the two, one positive and one negative, with the smallest absolute value of the energy. We will indicate the positive(negative)-energy solution with $s = +(-)$. ‡ Furthermore, we will restrict our analysis to energies that lie within the bulk gap. The quantum numbers that we will use to label the states are $s = \pm, j, k_z$. The secular problem yields the full knowledge of the eigenfunctions. In order to simplify the notation, in the following we rewrite the eigenfunction Eq. (10) as

$$\Psi_{s,j,k_z}(\rho, \varphi, z) = \frac{e^{ik_z z}}{2\pi} \begin{pmatrix} \Phi_{1,s,j,k_z}(\rho) e^{i(j-\frac{1}{2})\varphi} \\ \Phi_{2,s,j,k_z}(\rho) e^{i(j-\frac{1}{2})\varphi} \\ \Phi_{3,s,j,k_z}(\rho) e^{i(j+\frac{1}{2})\varphi} \\ \Phi_{4,s,j,k_z}(\rho) e^{i(j+\frac{1}{2})\varphi} \end{pmatrix}, \quad (13)$$

where the wavefunction obeys the normalisation condition $\sum_{i=1}^4 \int_0^R d\rho \rho |\Phi_{i,s,j,k_z}(\rho)|^2 = 1$.

3. Results

In order to understand the effect of a finite radius of the cylinder and how it affects the topologically protected surface states, we start from the large-radius limit.

3.1. Large-radius expansion

A natural length scale in this context is the effective Compton length $R_0 = \left| \frac{A}{m_0} \right|$. In the following we perform an expansion in R_0/R and find corrections to the asymptotic (large R) results obtained by Imura *et al.* [42]. To this aim, we make use of Hankel's asymptotic expansion for the Bessel function [43]

$$J_n(z) \approx \sqrt{\frac{2}{\pi z}} \left[P(n, z) \cos \left(z - \frac{1}{2}n\pi - \frac{1}{4}\pi \right) - Q(n, z) \sin \left(z - \frac{1}{2}n\pi - \frac{1}{4}\pi \right) \right]. \quad (14)$$

The functions $P(n, z)$ and $Q(n, z)$ are power serieses of $1/z$.

3.1.1. Zero axial momentum We start by considering the case of zero axial momentum ($k_z = 0$), with the goal to understand the j -dependence of the surface states. We will consider only one of the two secular equations, namely Eq. (12a) which can be recast as

$$\kappa_+ \Delta_- J_{j-\frac{1}{2}}(\kappa_+ R) J_{j+\frac{1}{2}}(\kappa_- R) - \kappa_- \Delta_+ J_{j+\frac{1}{2}}(\kappa_+ R) J_{j-\frac{1}{2}}(\kappa_- R) = 0. \quad (15)$$

For realistic materials, see Table 1, and small values of energies $E \ll |m_0|$, $\kappa_{\pm} = k \pm iq$ with $q > 0$. In the large-radius limit $qR \gg 1$, we keep only the terms proportional to

‡ In principle, we could introduce another integer quantum number to label the different solutions as in the case of a particle in a box.

$\exp(qR)$ in Eq. (14). The secular equation reduces to

$$\begin{aligned} \kappa_+ \Delta_- \left[P\left(j - \frac{1}{2}, \kappa_+ R\right) - iQ\left(j - \frac{1}{2}, \kappa_+ R\right) \right] \left[P\left(j + \frac{1}{2}, \kappa_- R\right) + iQ\left(j + \frac{1}{2}, \kappa_- R\right) \right] = \\ -\kappa_- \Delta_+ \left[P\left(j - \frac{1}{2}, \kappa_- R\right) + iQ\left(j - \frac{1}{2}, \kappa_- R\right) \right] \left[P\left(j + \frac{1}{2}, \kappa_+ R\right) - iQ\left(j + \frac{1}{2}, \kappa_+ R\right) \right]. \end{aligned} \quad (16)$$

Taking the zeroth order of the Hankel's expansion [i. e. $P(n, z) = 1$ and $Q(n, z) = 0$], the secular equation becomes

$$\kappa_+ \Delta_- + \kappa_- \Delta_+ = 0. \quad (17)$$

This equation has a zero-energy solution if $m_0/m_2 < 0$, i. e. when the system is in the topological phase.

Next, we consider the next two terms in the Hankel's expansion, that is $P(n, z) = 1 - (4n^2 - 1)(4n^2 - 9)/(128z^2)$ and $Q(n, z) = (4n^2 - 1)/(8z)$, and insert them into Eq. (16). After some tedious but otherwise standard algebra, we obtain the eigenenergies up to second-order in R_0/R

$$E = A \frac{j}{R} - \frac{A^2}{2m_0} \frac{j}{R^2}. \quad (18)$$

The first term is in agreement with Ref. [42], the second term gives the first correction to the asymptotic result. The other solution, with the opposite sign, $E = -Aj/R + \frac{A^2}{2m_0} \frac{j}{R^2}$ arises from solving Eq. (12b).

3.1.2. Finite axial momentum In this section we assume that $k_z R \gg 1$. Proceeding in the same way as for case $k_z = 0$, in zeroth-order in R_0/R the secular equation for the case of non-zero axial momentum reduces to

$$(\kappa_+ \Delta_- + \kappa_- \Delta_+)^2 + \frac{B^2}{A^2} k_z^2 (\Delta_+ - \Delta_-)^2 = 0. \quad (19)$$

This equation has the solutions

$$E = \pm Bk_z, \quad (20)$$

which represents the linear dispersion of the surface modes.

Considering the Hankel's expansion up to terms in $1/z^2$, that is $P(n, z) = 1 - (4n^2 - 1)(4n^2 - 9)/(128z^2)$ and $Q(n, z) = (4n^2 - 1)/(8z)$, we obtain the eigenenergies up to second order in R_0/R

$$E = \pm \left(Bk_z + \frac{1}{2} \frac{A^2 j^2}{Bk_z R^2} \right), \quad (21)$$

which corresponds to the Taylor expansion in second order in $1/(k_z R)$ of the result by Imura *et al.* [42], $E = \pm \sqrt{B^2 k_z^2 + A^2 j^2 / R^2}$. Notice that we are not allowed to take the $k_z \rightarrow 0$ limit, as this result has been derived assuming $k_z \gg 1/R$.

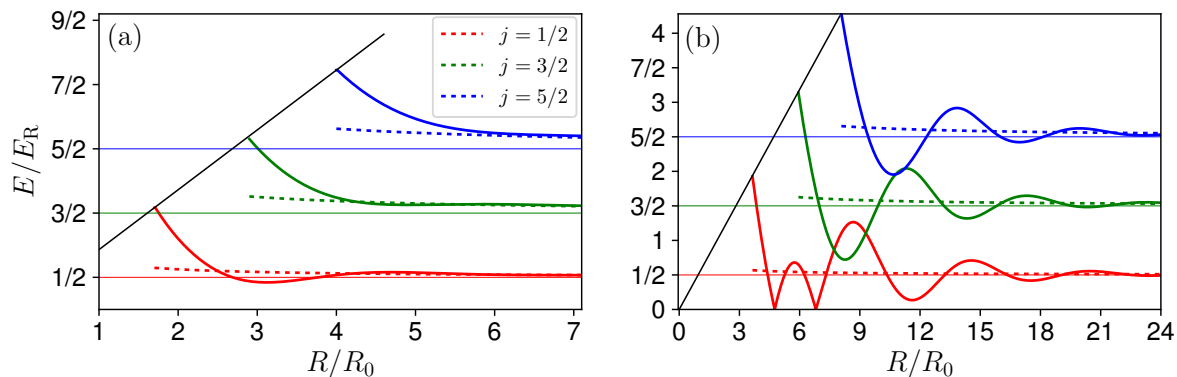


Figure 1. Eigenenergies in units of $E_R = A/R$ for a cylinder of (a) Bi_2Se_3 and (b) Bi_2Te_3 as a function of the radius R for $k_z = 0$. We only show the positive energies, i. e. $s = +$. Solid curves represent the numerical solution of Eqs. (12), whereas dashed curves represent the approximate large-radius result given in Eq. (18). Due to finite-size effects, for small and decreasing values of R the eigenenergies increase. For the model under consideration the bulk gap is given by $\min \left[|m_0|, \sqrt{-\frac{A^2}{m_2} \left(m_0 + \frac{1}{4} \frac{A^2}{m_2} \right)} \right]$, if the square root is real and by $|m_0|$ otherwise. Both for Bi_2Se_3 and Bi_2Te_3 the bulk gap is given by $\sqrt{-\frac{A^2}{m_2} \left(m_0 + \frac{1}{4} \frac{A^2}{m_2} \right)}$ and is indicated by a black solid line.

3.2. Numerical results

In this section we present numerical results for two different materials, namely Bi_2Se_3 and Bi_2Te_3 , using the parameters of Table 1. We use the following units for length and momentum, respectively,

$$R_0 = \left| \frac{A}{m_0} \right| \quad \text{and} \quad k_0 = \left| \frac{m_0}{B} \right|,$$

where $R_0 = 1.49$ nm for Bi_2Se_3 and 1.35 nm for Bi_2Te_3 .

Figure 1 shows how the eigenenergies in units of $E_R = A/R$ depend on the radius of the cylinder for the two materials and for three different values of j . Here we show only the positive energies, that is $s = +$. Solid curves refer to the exact result obtained by solving Eqs. (12), while the dashed curves refer to the large-radius analytic expression Eq. (18). We observe that the latter solutions approximate well the numerical results when $R \gtrsim 6R_0$ for Bi_2Se_3 , and when $R \gtrsim 20R_0$ for Bi_2Te_3 , respectively. For Bi_2Se_3 it is worthwhile noticing that at $R = 6R_0$, especially for $j = 3/2$ and $5/2$, the normalized eigenenergies have not yet reached the asymptotic ($R \gg R_0$) value [represented by the thin solid lines, see Eq. (18)]. On the other hand, when the radius of the cylinder is small, Fig. 1 shows an oscillatory behaviour, especially in the case of Bi_2Te_3 , that is more pronounced for smaller values of j , similarly to a spherical nanoparticle [36]. For Bi_2Te_3 , the effect of these oscillations are so large that, for some values of the radius, the surface-state energy goes to zero. This oscillatory behaviour is a consequence of the

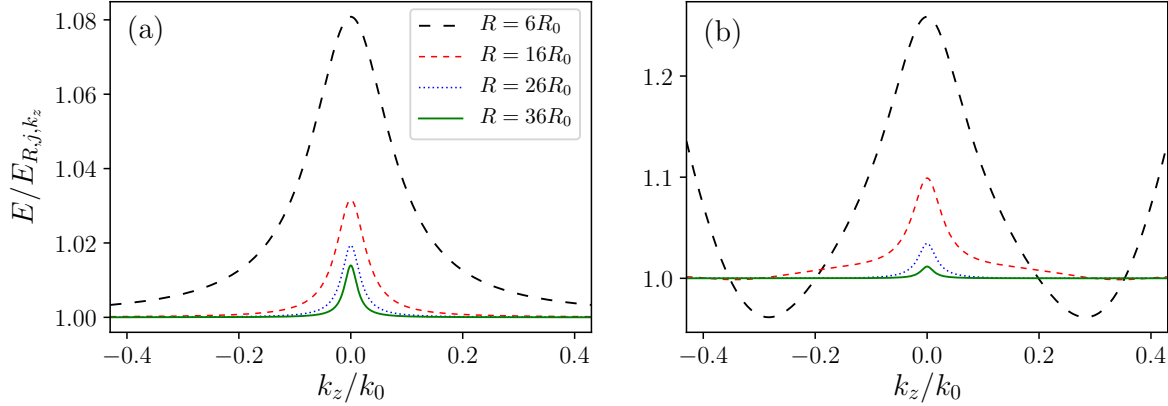


Figure 2. Eigenergies divided by the asymptotic value $E_{R,j,k_z} = \sqrt{B^2 k_z^2 + A^2 j^2 / R^2}$ as a function of wavevector k_z for a cylinder of (a) Bi_2Se_3 and (b) Bi_2Te_3 , for $j = \frac{1}{2}$ and different values of radius. In the case of Bi_2Te_3 , for $R = 6R_0$ the maximum value of k_z that yields a solution for surface states corresponds to $k_z = \pm 0.43k_0$ where $E = 1.14E_{R,j,k_z}$.

fact that the wavefunction is no longer localized on the surface of the cylinder. The oscillations are consistent with the results of Ref. [29] (see also Appendix B).

In Fig. 2 we show the positive eigenenergies, divided by the asymptotic value $E_{R,j,k_z} = \sqrt{B^2 k_z^2 + A^2 j^2 / R^2}$, as a function of wavevector k_z . Finite-size effects appear in this plot as deviations from unity of the normalized eigenenergies and are more pronounced for small values of k_z .

Since we have the full knowledge of the eigenfunctions, we can calculate the expectation values of any single-particle operator. The average of the radial coordinate in the state Ψ_{s,j,k_z} is simply given by

$$\langle \rho \rangle_{s,j,k_z} = \sum_{i=1}^4 \int_0^R d\rho 2\pi\rho^2 |\Phi_{i,s,j,k_z}(\rho)|^2, \quad (22)$$

and its variance by

$$\mathcal{D}\rho_{s,j,k_z} = \sqrt{\langle \rho^2 \rangle_{s,j,k_z} - \langle \rho \rangle_{s,j,k_z}^2}. \quad (23)$$

Figure 3 (top panels) shows that the average of the radial coordinate, $\langle \rho \rangle_{s,j,k_z}$, approaches R for large values of the radius as expected for topologically-protected surface states. The average of the radial position for both materials increases monotonically with the radius of the cylinder, showing weak oscillations only for the case of Bi_2Te_3 . As shown in Fig. 3 (bottom panels), the variance in itself approaches, in an oscillatory fashion, a constant value of the order of R_0 for large values of radius (the variance varies very little for $R \gtrsim 8R_0$ for Bi_2Se_3 and $R \gtrsim 24R_0$ for Bi_2Te_3). Since the value of R_0 is similar for the two materials ($R_0 = 1.5$ nm for Bi_2Se_3 and $R_0 = 1.35$ nm for Bi_2Te_3), we can conclude that in Bi_2Se_3 the asymptotic form of the surface states is reached for smaller values of the radius compared to Bi_2Te_3 .

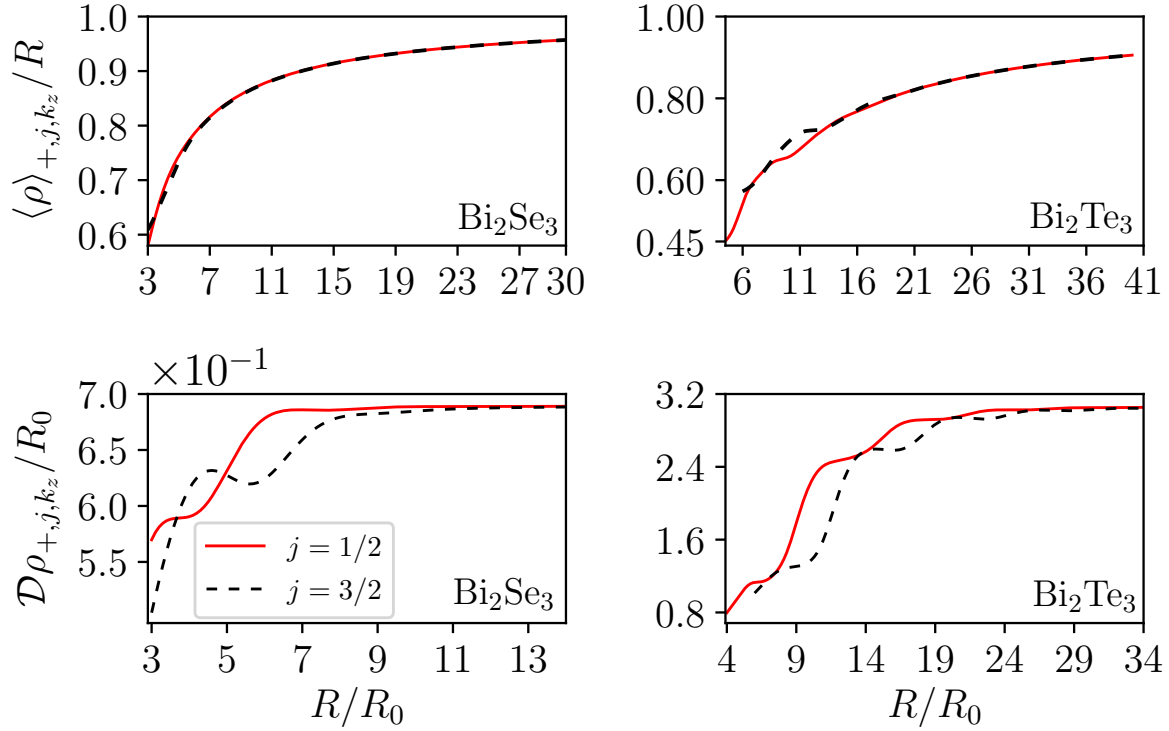


Figure 3. Average of the radial coordinate and the corresponding variance versus the radius of a cylinder of Bi_2Se_3 (left panels) and Bi_2Te_3 (right panels) for $k_z = 0$ and $j = \frac{1}{2}$ (solid line) and $j = \frac{3}{2}$ (dashed line).

3.3. Optical transitions in cylindrical topological insulators

The Hamiltonian in Eq. (1) can be written as:

$$H_0 = (m_0 + m_1 k_z^2 + m_2 (k_x^2 + k_y^2)) \tau_z \otimes \sigma_0 + B k_z \tau_x \otimes \sigma_z + A k_x \tau_x \otimes \sigma_x + A k_y \tau_x \otimes \sigma_y, \quad (24)$$

where σ_i and τ_i are Pauli matrices in spin and orbital-pseudo-spin space, respectively. The velocity operator $\mathbf{v} = \partial H_0 / \partial \mathbf{k}|_{\mathbf{k}=0}$ for the the Hamiltonian (24) and the optical dipole operator $\mathbf{d} = e\mathbf{r}$ are connected by the fundamental relation [44]:

$$\mathbf{d}_{\tau\sigma,\tau'\sigma'} = \tau \frac{ie}{2m_0} \mathbf{v}_{\tau\sigma,\tau'\sigma'}, \quad (25)$$

where $\mathbf{d}_{\tau\sigma,\tau'\sigma'} = \langle \tau'\sigma' | e\mathbf{r} | \tau\sigma \rangle$ and $\mathbf{v}_{\tau\sigma,\tau'\sigma'} = \langle \tau'\sigma' | \mathbf{v} | \tau\sigma \rangle$. Here $|\tau\sigma\rangle$ represents the basis functions in the orbital and spin space of the Hamiltonian H_0 defined in Eq. (1), and τ is the eigenvalue of τ_z associated with the eigenstate $|\tau\sigma\rangle$. Following the procedure of Ref. [36], we straightforwardly obtain

$$\mathbf{d} = e\mathbf{r} \tau_0 \otimes \sigma_0 + \frac{eB}{2m_0} \tau_y \otimes \sigma_z \hat{z} + \frac{eA}{2m_0} \tau_y \otimes \sigma_y \hat{y} + \frac{eA}{2m_0} \tau_y \otimes \sigma_x \hat{x}, \quad (26)$$

for the optical-dipole operator in envelope function representation. The expression given in Eq. (26) accounts on the same footing for both envelope-function-mediated

(sometimes called *intraband*) transitions, which are associated with the first term on the r.h.s., and basis-function-mediated (*interband*) transitions, which are subsumed in the remaining three terms. The optical dipole matrix elements are given by

$$\mathbf{d}_{s,j,k_z}^{s',j',k'_z} = \int dz \int_0^R \rho d\rho \int_0^{2\pi} d\varphi \Psi_{s',j',k'_z}^\dagger(\rho, \varphi, z) \mathbf{d}(\rho, \varphi, z) \Psi_{s,j,k_z}(\rho, \varphi, z).$$

Using Eq. (10) and performing the integrals over φ and z , we obtain

$$(d_x + id_y)_{s,j,k_z}^{s',j',k'_z} = \delta_{k_z,k'_z} \delta_{j',j+1} \left[e \sum_{i=1}^4 (\mathcal{R}_{ii})_{s,j,k_z}^{s',j+1,k_z} - \frac{ieA}{m_0} \left((\mathcal{S}_{14})_{s,j,k_z}^{s',j+1,k_z} - (\mathcal{S}_{23})_{s,j,k_z}^{s',j+1,k_z} \right) \right], \quad (27)$$

and

$$(d_x - id_y)_{s,j,k_z}^{s',j',k'_z} = \delta_{k_z,k'_z} \delta_{j',j-1} \left[e \sum_{i=1}^4 (\mathcal{R}_{ii})_{s,j,k_z}^{s',j-1,k_z} - \frac{ieA}{m_0} \left((\mathcal{S}_{32})_{s,j,k_z}^{s',j-1,k_z} - (\mathcal{S}_{41})_{s,j,k_z}^{s',j-1,k_z} \right) \right], \quad (28)$$

where we have defined the overlap integrals

$$(\mathcal{S}_{mn})_{s,j,k_z}^{s',j',k'_z} = \int_0^R d\rho \rho \Phi_{m,s',j',k'_z}^*(\rho) \Phi_{n,s,j,k_z}(\rho) \quad (29)$$

and the matrix elements of radial position

$$(\mathcal{R}_{mn})_{s,j,k_z}^{s',j',k'_z} = \int_0^R d\rho \rho^2 \Phi_{m,s',j',k'_z}^*(\rho) \Phi_{n,s,j,k_z}(\rho). \quad (30)$$

For circular polarization in the plane perpendicular to the nanowire axis, we find the conventional selection rule $j' = j \pm 1$, which is mandated by the conservation of total-angular-momentum projection (including the photon's) parallel to the nanowire axis. In addition, linear momentum k_z parallel to the nanowire axis is conserved in any optical transition. The energy threshold for absorption is associated with transitions between $(s' = +, j = \pm 1/2, k'_z = 0)$ and $(s = -, j \mp 1/2, k_z = 0)$. At the subband edge ($k_z = 0$ and $k'_z = 0$) for $d_x + id_y$ only the overlap integral $(\mathcal{S}_{14})_{-,-1/2,0}^{+,1/2,0}$ is non-vanishing for absorption, while for emission the only non-vanishing overlap integral is $(\mathcal{S}_{23})_{+,-1/2,0}^{-,1/2,0}$. For the opposite polarization, namely $d_x - id_y$, the non vanishing overlap integrals at the band edge are: $(\mathcal{S}_{32})_{-,-1/2,0}^{+,-1/2,0}$ for absorption and $(\mathcal{S}_{41})_{+,1/2,0}^{-,-1/2,0}$ for emission, respectively. The overlap integrals relevant for the absorption threshold are shown in Fig. 4 as a function of the radius of the wire. It needs to be noticed that also the matrix elements of the radial position $(\mathcal{R}_{mn})_{s,j,k_z}^{s',j',k'_z}$ contribute both to absorption and emission. The sum of these matrix elements for the case of absorption is shown in Fig. 5 as a function of the radius of the wire. The finite radius of the nanowire does not affect the selection rules but leads to significant quantitative changes of the dipole matrix elements.

Matrix elements of the optical-dipole component parallel to the nanowire axis are

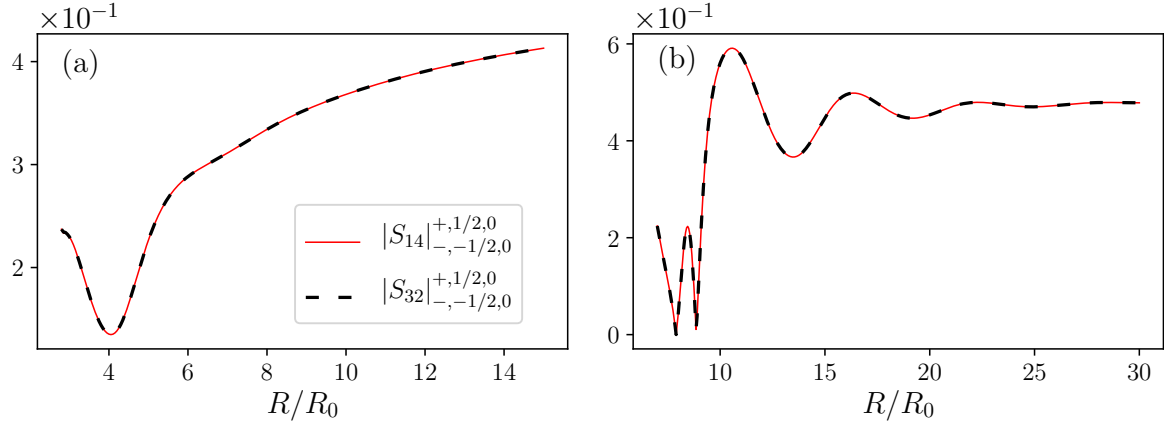


Figure 4. Overlap integrals entering the dipole matrix element relevant for absorption for circularly-polarised light as a function of the radius of the cylinder of (a) Bi_2Se_3 and (b) Bi_2Te_3 for $k_z = k'_z = 0$. We observe that, $|S_{41}|_{-, -1/2, 0}^{+, 1/2, 0} = |S_{23}|_{-, -1/2, 0}^{+, 1/2, 0} = 0$ for all values of R considered. For panel (a), the smallest value of radius considered is the one corresponding to $E \simeq |m_0|$. For panel (b), instead, the smallest radius considered is the one for which the eigenenergy, given by the solution of Eq. (12a), passes through zero (corresponding to the kink at $R \simeq 7R_0$ in Fig. 1).

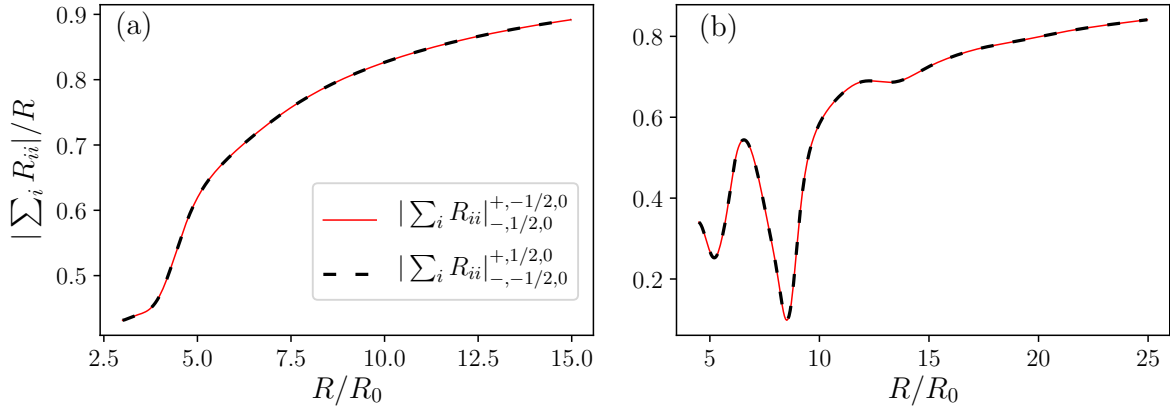


Figure 5. Dependence of $\sum_{i=1}^4 \mathcal{R}_{ii}$ on the radius of the cylinder of (a) Bi_2Se_3 and (b) Bi_2Te_3 for $k_z = k'_z = 0$.

given by

$$(d_z)_{s,j,k_z}^{s',j',k'_z} = \left\{ e \sum_{i=1}^4 (\mathcal{S}_{ii})_{s,j,k_z}^{s',j',k'_z} \int dz z \frac{e^{i(k_z - k'_z)z}}{2\pi} + \delta_{k_z, k'_z} \frac{ieB}{2m_0} \left[(\mathcal{S}_{21})_{s,j,k_z}^{s',j',k'_z} - (\mathcal{S}_{12})_{s,j,k_z}^{s',j',k'_z} + (\mathcal{S}_{34})_{s,j,k_z}^{s',j',k'_z} - (\mathcal{S}_{43})_{s,j,k_z}^{s',j',k'_z} \right] \right\} \delta_{j', j}. \quad (31)$$

The first term on the r.h.s. of Eq. (31) is ill-defined because the envelope functions are not localized in their dependence on the z coordinate and, hence, the dipole approximation

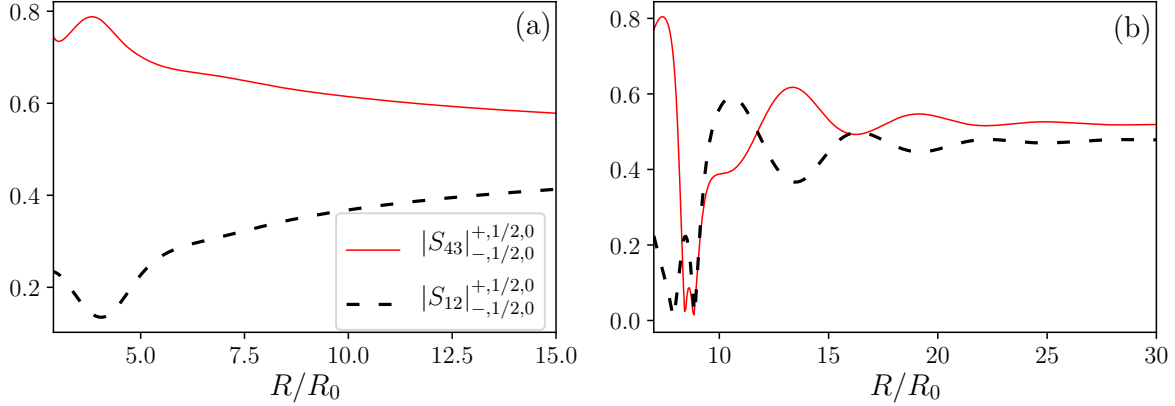


Figure 6. Overlap integrals entering the dipole matrix element relevant for absorption for linearly-polarised (longitudinal) light as a function of the radius of the cylinder of (a) Bi_2Se_3 and (b) Bi_2Te_3 for $k_z = k'_z = 0$.

is not valid. However, the remaining basis-function-mediated contributions describe valid optical transitions. For these, both linear momentum k_z and the total-angular-momentum projection j parallel to the nanowire axis are the same for initial and final states involved in optical transitions. For states at the energy threshold of absorption, we find that the only non vanishing overlap integrals are $(\mathcal{S}_{12})_{-, \pm 1/2, 0}^{+, \pm 1/2, 0}$ and $(\mathcal{S}_{43})_{-, \pm 1/2, 0}^{+, \pm 1/2, 0}$, while for emission the non vanishing overlap integrals are $(\mathcal{S}_{21})_{+, \pm 1/2, 0}^{-, \pm 1/2, 0}$ and $(\mathcal{S}_{34})_{+, \pm 1/2, 0}^{-, \pm 1/2, 0}$. The overlap integrals relevant for absorption are shown in Fig. 6. Again, the selection rules for optical transitions are consistent with the basic symmetries associated with a cylindrical-nanowire geometry, and finite-size effects are manifested as significant quantitative changes in the magnitude of dipole matrix elements.

4. Conclusions

In this paper we have studied a nanowire made of TI. In particular, we have provided the analytical form of the energy eigenfunctions, which is central to the derivation of an analytical secular equation for the eigenenergies. This secular equation, on one hand, enables an analytical expansion for large radii and, on the other hand, is amenable to straightforward numerical solution. We study the dependence of the eigenenergies on the radius of the wire and we find oscillations as a function of the radius, which are very pronounced for Bi_2Te_3 . The analytical form of the energy eigenfunctions enables the computation of the matrix elements of any single-particle operator. We have considered the optical dipole matrix elements. While we find the usual selection rules for absorption/emission, the value of the matrix elements is strongly dependent on the radius of the cylinder.

Appendix A. Secular equation for confined states

In this Appendix we provide the detailed derivation of the secular equation for the state of the TI cylinder. Acting with the Hamiltonian (2) on the wave function Eq. (6) and looking for eigenfunctions with energy E , we obtain

$$\begin{pmatrix} m_{\perp}+m_{-}(j,k_z)-E & Bk_z & 0 & -iA[\partial_{\rho}+\frac{1}{\rho}(j+\frac{1}{2})] \\ Bk_z & -[m_{\perp}+m_{-}(j,k_z)+E] & -iA[\partial_{\rho}+\frac{1}{\rho}(j+\frac{1}{2})] & 0 \\ 0 & -iA[\partial_{\rho}-\frac{1}{\rho}(j-\frac{1}{2})] & m_{\perp}+m_{+}(j,k_z)-E & -Bk_z \\ -iA[\partial_{\rho}-\frac{1}{\rho}(j-\frac{1}{2})] & 0 & -Bk_z & -[m_{\perp}+m_{+}(j,k_z)+E] \end{pmatrix} \begin{pmatrix} \Phi_1(\rho) \\ \Phi_2(\rho) \\ \Phi_3(\rho) \\ \Phi_4(\rho) \end{pmatrix} = 0, \quad (\text{A.1})$$

where we have defined $m_{\pm}(j, k_z) = m_2 \frac{1}{\rho^2} (j \pm \frac{1}{2})^2 + m_1 k_z^2$. To solve the eigensystem Eq. (A.1) we make the *Ansatz*

$$\begin{pmatrix} \Phi_1(\rho) \\ \Phi_2(\rho) \\ \Phi_3(\rho) \\ \Phi_4(\rho) \end{pmatrix} = \begin{pmatrix} c_1 J_{j-\frac{1}{2}}(\kappa\rho) \\ c_2 J_{j-\frac{1}{2}}(\kappa\rho) \\ c_3 J_{j+\frac{1}{2}}(\kappa\rho) \\ c_4 J_{j+\frac{1}{2}}(\kappa\rho) \end{pmatrix}, \quad (\text{A.2})$$

where $J_n(z)$ is a Bessel function of the first kind and κ and the coefficients c_1, \dots, c_4 need to be determined. Substituting the *Ansatz* Eq. (A.2) in (A.1), we obtain the following equation for the coefficients

$$\begin{pmatrix} -\left(\kappa^2 + \frac{m_1}{m_2} k_z^2 + \frac{m_0 - E}{m_2}\right) & -\frac{Bk_z}{m_2} & 0 & i\frac{A\kappa}{m_2} \\ \frac{Bk_z}{m_2} & -\left(\kappa^2 + \frac{m_1}{m_2} k_z^2 + \frac{m_0 + E}{m_2}\right) & -i\frac{A\kappa}{m_2} & 0 \\ 0 & -i\frac{A\kappa}{m_2} & -\left(\kappa^2 + \frac{m_1}{m_2} k_z^2 + \frac{m_0 - E}{m_2}\right) & \frac{Bk_z}{m_2} \\ i\frac{A\kappa}{m_2} & 0 & -\frac{Bk_z}{m_2} & -\left(\kappa^2 + \frac{m_1}{m_2} k_z^2 + \frac{m_0 + E}{m_2}\right) \end{pmatrix} \begin{pmatrix} c_1 \\ c_2 \\ c_3 \\ c_4 \end{pmatrix} = 0. \quad (\text{A.3})$$

Equation (A.3) has non trivial solutions for

$$\left(\kappa^2 + \frac{m_1}{m_2} k_z^2 + \frac{m_0}{m_2}\right)^2 + \frac{A^2}{m_2^2} \kappa^2 + \frac{B^2}{m_2^2} k_z^2 - \frac{E^2}{m_2^2} = 0 \quad (\text{A.4})$$

which yields[§]

$$\kappa = \kappa_{\pm} = \sqrt{-\left(\frac{m_0}{m_2} + \frac{A^2}{2m_2^2} + \frac{m_1}{m_2} k_z^2\right) \pm \sqrt{\frac{A^4}{4m_2^4} + \frac{E^2}{m_2^2} + \frac{A^2 m_0}{m_2^3} + \left(\frac{A^2}{m_2^2} \frac{m_1}{m_2} - \frac{B^2}{m_2^2}\right) k_z^2}}. \quad (\text{A.5})$$

There are four independent solutions for $(c_1, c_2, c_3, c_4)^T$ and are given by

$$\left(\frac{iA\kappa_{\pm}}{\Delta_{\pm}}, 0, \frac{Bk_z}{\Delta_{\pm}}, 1\right)^T, \quad (\text{A.6})$$

$$\left(-\frac{Bk_z}{\Delta_{\pm}}, 1, -\frac{iA\kappa_{\pm}}{\Delta_{\pm}}, 0\right)^T, \quad (\text{A.7})$$

[§] The negative sign for the outer square root does not give a different solution and therefore should not be considered due to the property of the Bessel's functions: $J_n(z) = (-1)^n J_n(-z)$ for integer n .

where we have introduced the following abbreviation $\Delta_{\pm} = m_2\kappa_{\pm}^2 + m_1k_z^2 + m_0 - E$. The general solution with quantum numbers k_z , j and E can therefore be written as

$$\Psi(\rho, \varphi, z) = \frac{e^{ik_z z}}{\sqrt{2\pi}} \sum_{s=\pm} \left\{ \alpha_s \begin{pmatrix} \frac{iA\kappa_s}{\Delta_s} J_{j-\frac{1}{2}}(\kappa_s\rho) e^{i(j-\frac{1}{2})\varphi} \\ 0 \\ \frac{Bk_z}{\Delta_s} J_{j+\frac{1}{2}}(\kappa_s\rho) e^{i(j+\frac{1}{2})\varphi} \\ J_{j+\frac{1}{2}}(\kappa_s\rho) e^{i(j+\frac{1}{2})\varphi} \end{pmatrix} + \beta_s \begin{pmatrix} -\frac{Bk_z}{\Delta_s} J_{j-\frac{1}{2}}(\kappa_s\rho) e^{i(j-\frac{1}{2})\varphi} \\ J_{j-\frac{1}{2}}(\kappa_s\rho) e^{i(j-\frac{1}{2})\varphi} \\ -\frac{iA\kappa_s}{\Delta_s} J_{j+\frac{1}{2}}(\kappa_s\rho) e^{i(j+\frac{1}{2})\varphi} \\ 0 \end{pmatrix} \right\}. \quad (\text{A.8})$$

Assuming a hard-wall cylindrical confinement potential of radius R , we need to impose the boundary condition $\Psi(R, \varphi, z) = 0$ which leads to the following system of equations:

$$\begin{pmatrix} \frac{iA\kappa_+}{\Delta_+} J_{j-\frac{1}{2}}(\kappa_+R) & -\frac{Bk_z}{\Delta_+} J_{j-\frac{1}{2}}(\kappa_+R) & \frac{iA\kappa_-}{\Delta_-} J_{j-\frac{1}{2}}(\kappa_-R) & -\frac{Bk_z}{\Delta_-} J_{j-\frac{1}{2}}(\kappa_-R) \\ 0 & J_{j-\frac{1}{2}}(\kappa_+R) & 0 & J_{j-\frac{1}{2}}(\kappa_-R) \\ \frac{Bk_z}{\Delta_+} J_{j+\frac{1}{2}}(\kappa_+R) & -\frac{iA\kappa_+}{\Delta_+} J_{j+\frac{1}{2}}(\kappa_+R) & \frac{Bk_z}{\Delta_-} J_{j+\frac{1}{2}}(\kappa_-R) & -\frac{iA\kappa_-}{\Delta_-} J_{j+\frac{1}{2}}(\kappa_-R) \\ J_{j+\frac{1}{2}}(\kappa_+R) & 0 & J_{j+\frac{1}{2}}(\kappa_-R) & 0 \end{pmatrix} \begin{pmatrix} \alpha_+ \\ \beta_+ \\ \alpha_- \\ \beta_- \end{pmatrix} = 0. \quad (\text{A.9})$$

We then obtain the secular equation

$$\begin{aligned} & \left[\kappa_+\Delta_- J_{j-\frac{1}{2}}(\kappa_-R) J_{j+\frac{1}{2}}(\kappa_+R) - \kappa_-\Delta_+ J_{j-\frac{1}{2}}(\kappa_+R) J_{j+\frac{1}{2}}(\kappa_-R) \right] \times \\ & \left[\kappa_+\Delta_- J_{j-\frac{1}{2}}(\kappa_+R) J_{j+\frac{1}{2}}(\kappa_-R) - \kappa_-\Delta_+ J_{j-\frac{1}{2}}(\kappa_-R) J_{j+\frac{1}{2}}(\kappa_+R) \right] + \\ & \frac{B^2}{A^2} k_z^2 (\Delta_+ - \Delta_-)^2 J_{j-\frac{1}{2}}(\kappa_-R) J_{j-\frac{1}{2}}(\kappa_+R) J_{j+\frac{1}{2}}(\kappa_-R) J_{j+\frac{1}{2}}(\kappa_+R) = 0. \end{aligned} \quad (\text{A.10})$$

Notice that the term in the third line of Eq. (A.10) vanishes for $k_z = 0$. By simple algebraic manipulations, Eq. (A.10) can be cast in the form of Eq. (11).

Appendix B. Small-radius limit

In section 3.2 we found interesting finite-size effects for small values of the radius R , such as the oscillatory behaviour of the eigenenergies. In order to understand the origin of the oscillations in Fig. 1, here we use the Hankel's asymptotic expansion [Eq. (14)], but without approximating the trigonometric functions, and solve the secular equation at each given order. The plot of the eigenenergy as a function of R , obtained by taking into account only the first order in $1/z$ [$P(n, z) = 1$ and $Q(n, z) = (4n^2 - 1)/(8z)$], is shown in Fig. B1 as a dashed black curve: it is found to agree remarkably well with the full numerical results (solid red curve). The expansion up to second order in $1/z$ (not shown) [$P(n, z) = 1 - (4n^2 - 1)(4n^2 - 9)/(128z^2)$ and $Q(n, z) = (4n^2 - 1)/(8z)$] is practically indistinguishable from the full numerical results.

References

- [1] Fu L, Kane C L and Mele E J 2007 Topological insulators in three dimensions *Phys. Rev. Lett.* **98** 106803

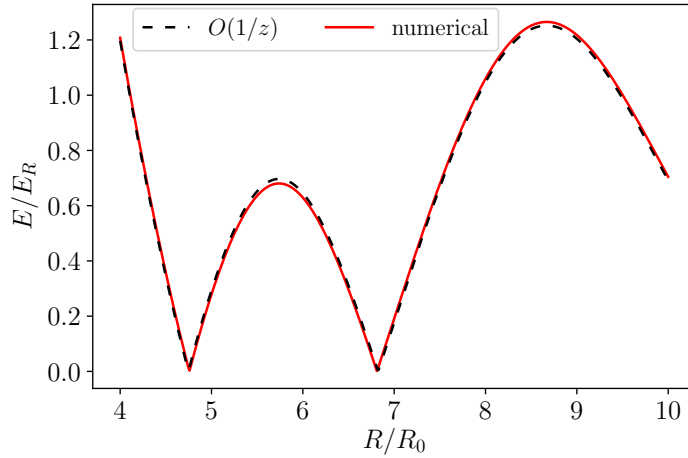


Figure B1. Eigenenergies with $j = \frac{1}{2}$ and $s = +$ for a cylinder of Bi_2Te_3 as a function of radius for $k_z = 0$. The solid red curve is the exact numerical solution of Eq. (11) while the dashed black curves is obtained by means of the Hankel's expansion at first order in $1/z$.

- [2] Hasan M Z and Kane C L 2010 Colloquium: Topological insulators *Rev. Mod. Phys.* **82** 3045
- [3] Qi X L and Zhang S C 2011 Topological insulators and superconductors *Rev. Mod. Phys.* **83** 1057
- [4] Hasan M Z and Moore J E 2011 Three-dimensional topological insulators *Annu. Rev. Condens. Matter Phys.* **2** 55
- [5] Ando Y 2013 Topological Insulator Materials *J. Phys. Soc. Jpn.* **82** 102001
- [6] Lee D H 2009 Surface States of Topological Insulators: The Dirac Fermion in Curved Two-Dimensional Spaces *Phys. Rev. Lett.* **103** 196804
- [7] Parente V, Lucignano P, Vitale P, Tagliacozzo A and Guinea F 2011 Spin connection and boundary states in a topological insulator *Phys. Rev. B* **83** 075424
- [8] Imura K I, Yoshimura Y, Takane Y and Fukui T 2012 Spherical topological insulator *Phys. Rev. B* **86** 235119
- [9] Cho S, Dellabetta B, Zhong R, Schneeloch J, Liu T, Gu G, Gilbert M J and Mason N 2015 Aharonov-Bohm oscillations in a quasi-ballistic three-dimensional topological insulator nanowire *Nature Communications* **6** 7634
- [10] Kim M, Kim J, Hou Y, Yu D, Doh Y J, Kim B, Kim K W and Suh J 2019 Nanomechanical characterization of quantum interference in a topological insulator nanowire *Nature Communications* **10** 4522
- [11] Munning F, Breunig O, Legg H F, Roitsch S, Fan D, Röbller M, Rosch A and Ando Y 2019 Quantum confinement of the Dirac surface states in topological-insulator nanowires *arXiv:1910.07863*
- [12] Tian M, et al 2013 Dual evidence of surface dirac states in thin cylindrical topological insulator Bi_2Te_3 nanowires *Scientific Reports* **3** 1212
- [13] Hamdou B, Gooth J, Dorn A, Pippel E and Nielsch K 2013 Surface state dominated transport in topological insulator Bi_2Te_3 nanowires *App. Phys. Lett.* **103** 193107
- [14] Safdar M et al 2013 Topological surface transport properties of single-crystalline SnTe nanowire *Nano Lett.* **13** 5344
- [15] Bäßler S, et al 2015 One-dimensional edge transport on the surface of cylindrical $\text{Bi}_x\text{Te}_3 - y\text{Se}_y$ nanowires in transverse magnetic fields *App. Phys. Lett.* **107** 181602
- [16] Arango Y C et al 2016 Quantum transport and nano angle-resolved photoemission spectroscopy on the topological surface states of single Sb_2Te_3 nanowires *Scientific Reports* **6** 29493

- [17] Ziegler J et al 2018 Probing spin helical surface states in topological HgTe nanowires *Phys. Rev. B* **97** 035157
- [18] Bhattacharyya B, Sharma A, Awana V P S, Senguttuvan T D and Husale S 2017 FIB synthesis of Bi₂Se₃ 1D nanowires demonstrating the co-existence of Shubnikov-de Haas oscillations and linear magnetoresistance *Jour. of Phys. Con. Matt.* **29** 07LT01
- [19] Peng H et al 2009 AharonovBohm interference in topological insulator nanoribbons *Nat. Mat.* **9** 225
- [20] Xiu F et al 2011 Manipulating surface states in topological insulator nanoribbons *Nat. Nanotech.* **6**, 216
- [21] Hong S S, Cha J J, Kong D and Cui Y 2012 Ultra-low carrier concentration and surface-dominant transport in antimony-doped Bi₂Se₃ topological insulator nanoribbons *Nat. Comm.* **3** 757
- [22] Wang Z, Qiu R L J, Lee C H, Zhang Z and Gao X P A 2013 Ambipolar surface conduction in ternary topological insulator Bi₂(Te_{1-x}Se_x)₃ nanoribbons *ACS Nano* **7** 2126
- [23] Jauregui L A, Pettes M T, Rokhinson L P, Shi L and Chen Y P 2015 Gate tunable relativistic mass and Berry's phase in topological insulator nanoribbon field effect devices *Scientific Reports* **5** 8452
- [24] Dufouleur J et al 2017 Weakly-coupled quasi-1d helical modes in disordered 3d topological insulator quantum wires *Scientific Reports* **7** 45276
- [25] Kunakova G et al 2018 Bulk-free topological insulator Bi₂Se₃ nanoribbons with magnetotransport signatures of Dirac surface states *Nanoscale* **10** 19595
- [26] Hong S S, Zhang Y, Cha J J, Qi X L and Cui Y 2014 One-dimensional helical transport in topological insulator nanowire interferometers *Nano Lett.* **14** 2815
- [27] de Juan F, Ilan R, and Bardarson J H 2014 Robust Transport Signatures of Topological Superconductivity in Topological Insulator Nanowires *Phys. Rev. Lett.* **113**107003
- [28] Cook A and Franz M 2011 Majorana fermions in a topological-insulator nanowire proximity-coupled to an *s*-wave superconductor *Phys. Rev. B* **84** 201105
- [29] Iorio P, Perroni C A and Cataudella V 2016 Quantum interference effects in Bi₂Se₃ topological insulator nanowires with variable cross-section lengths *The European Physical Journal B* **89** 97
- [30] Hong S S, Kong D, and Cui Y 2014 Topological insulator nano-structures *MRS Bull.* **39** 873
- [31] Zhou B, Lu H Z, Chu R L, Shen S Q and Niu Q 2008 Finite Size Effects on Helical Edge States in a Quantum Spin-Hall System *Phys. Rev. Lett.* **101** 246807
- [32] Linder J, Yokoyama T and Sudbø A 2009 Anomalous finite size effects on surface states in the topological insulator Bi₂Se₃ *Phys. Rev. B* **80** 205401
- [33] Liu C X, Zhang H, Yan B, Qi X L, Frauenheim T, Dai X, Fang Z and Zhang S C 2010 Oscillatory crossover from two-dimensional to three-dimensional topological insulators *Phys. Rev. B* **81** 041307
- [34] Imura K I, Okamoto M, Yoshimura Y, Takane Y and Ohtsuki T 2012 Finite-size energy gap in weak and strong topological insulators *Phys. Rev. B* **86** 245436
- [35] Kotulla M and Zülicke U 2017 Manipulating topological-insulator properties using quantum confinement *New J. Phys.* **19**, 073025
- [36] Gioia L, Christie M G, Zülicke U, Governale M and Sneyd A J 2019 Spherical topological insulator nanoparticles: Quantum size effects and optical transitions *Phys. Rev. B* **100** 205417
- [37] Zhang Y and Vishwanath A 2010 Anomalous aharonov-bohm conductance oscillations from topological insulator surface states *Phys. Rev. Lett.* **105** 206601
- [38] Bardarson J H, Brouwer P W and Moore J E 2010 Aharonov-bohm oscillations in disordered topological insulator nanowires *Phys. Rev. Lett.* **105** 156803
- [39] Zhang H, Liu C X, Qi X L, Dai X, Fang Z and Zhang S C 2009 Topological insulators in Bi₂Se₃, Bi₂Te₃ and Sb₂Te₃ with a single Dirac cone on the surface *Nat. Phys.* **82** 438
- [40] Liu C X, Qi X L, Zhang H, Dai X, Fang Z and Zhang S C 2010 Model Hamiltonian for topological insulators *Phys. Rev. B* **82** 045122

- [41] Nechaev I A and Krasovskii E E 2016 Relativistic $\mathbf{k} \cdot \mathbf{p}$ Hamiltonians for centrosymmetric topological insulators from *ab initio* wave functions *Phys. Rev. B* **94** 201410
- [42] Imura K I, Takane Y and Tanaka A 2011 Spin Berry phase in anisotropic topological insulators *Phys. Rev. B* **84** 195406
- [43] Abramowitz M and Stegun I A 1964 *Handbook of Mathematical Functions* (Dover, New York)
- [44] Haug H and Koch S W 2009 *Quantum Theory of the Optical and Electronic Properties of Semiconductors: Fifth Edition* (World Scientific Publishing Company)